

Transmission Efficiency in Complex-Shaped Waveguide using Real Metals^{*)}

Yoshihisa FUJITA¹⁾, Soichiro IKUNO²⁾ and Hiroaki NAKAMURA^{1,3)}

¹⁾*Department of Energy Engineering and Science, Nagoya University, 322-6 Oroshi, Toki, Gifu 509-5292, Japan*

²⁾*Tokyo University of Technology, 1404-1 Katakura, Hachioji, Tokyo 192-0982, Japan*

³⁾*National Institute for Fusion Science, 322-6 Oroshi, Toki, Gifu 509-5292, Japan*

(Received 10 December 2013 / Accepted 23 March 2014)

The two-dimensional meshless time-domain method (2D-MTDM) was used to simulate the electromagnetic wave propagation phenomena in complex-shaped waveguides considering the influence of metals and to numerically investigate the relation of the dispersion medium with the attenuation rate. The simulation results suggest that the waveguide with grooves is strongly affected by the frequency of the propagating wave than the waveguide without grooves because the wave propagating in the waveguide with the grooves penetrates deep into the metal compared with the waveguide without grooves. The transmission loss for the curved waveguide is greater than that for the straight waveguide.

© 2014 The Japan Society of Plasma Science and Nuclear Fusion Research

Keywords: millimeter wave, MTDM, dispersive media, Drude model, RC method

DOI: 10.1585/pfr.9.3401074

1. Introduction

In the Large Helical Device (LHD), plasma is heated using the resonance of the millimeter waves. The millimeter waves propagate on a long transmission path that bends several times. In the waveguides without grooves, transmission loss occurs because of the eddy currents induced into the metal constructing the waveguide. Thus, for efficient heating, it is necessary to reduce the transmission loss in the path.

For the transmission of millimeter waves, corrugated waveguides are used [1]. The transmission efficiency of the corrugated waveguides has been investigated [2–4]. The waveguide walls are assumed metallic, and the perfect electric conductor (PEC) was adopted as the boundary conditions to implement this assumption. However, the Joule heat was not generated because PEC has no electroresistance. In fact, theoretically, there is no energy loss if the PEC is adopted. The Drude model supports the complex dielectric constant required for the metals to be used as the waveguide walls [5].

The purpose of this paper is to develop a two-dimensional meshless time-domain method (2D-MTDM) code on the basis of the Drude model and the recursive convolution (RC) method. In addition, the influence of the dispersion metal and the grooves on the transmission efficiency is investigated by calculating the electromagnetic wave propagation in the corrugated waveguide.

2. Numerical Method

Generally, the finite difference time domain method (FDTD) is used to analyze electromagnetic wave propagation. However, the analytic domain must be divided into orthogonal meshes if FDTD is used for the simulations. In this paper, the MTDM is adopted to study the propagation of electromagnetic waves in complex domains. In addition, the Drude model is adopted by the RC method for the dispersion model.

2.1 Meshless time-domain method

The governing equations for the two-dimensional wave propagation phenomena are defined by following equations:

$$\frac{\partial \mathbf{E}}{\partial t} = -\frac{\sigma}{\varepsilon} \mathbf{E} + \frac{1}{\varepsilon} \nabla \times \mathbf{H}, \quad (1)$$

$$\frac{\partial \mathbf{H}}{\partial t} = -\frac{1}{\mu} \nabla \times \mathbf{E}. \quad (2)$$

Here, \mathbf{E} denotes the electric field and \mathbf{H} denotes the magnetic field. Moreover, ε , μ , and σ denote the permittivity, permeability, and electroconductivity, respectively. As mentioned above, the basic concept of MTDM is the same as that of FDTD. The time domain is discretized by the leapfrog algorithm. On the other hand, the space is discretized by the shape functions obtained with the meshless method. To this end, the nodes, $\mathbf{r}_1, \mathbf{r}_2, \dots$, and \mathbf{r}_N , are scattered in the analytical domain and are on the boundaries. Subsequently, we consider an arbitrary function $u(\mathbf{r})$. The value of the function $u(\mathbf{r})$ on node \mathbf{r}_i is u_i . Then, the function $u(\mathbf{r})$ is interpolated by the shape functions $\phi_i(\mathbf{r})$ as

author's e-mail: teamMD@nifs.ac.jp

^{*)} This article is based on the presentation at the 23rd International Toki Conference (ITC23).

follows:

$$\hat{u}(\mathbf{r}) = \sum_{i=1}^N u_i \phi_i(\mathbf{r}). \quad (3)$$

Here, $\hat{u}(\mathbf{r})$ denotes the interpolation function of $u(\mathbf{r})$, and $\phi_i(\mathbf{r})$ denotes the shape function corresponding to the node \mathbf{r}_i . In this paper, we adopted the shape functions obtained by the radial point interpolation method (RPIM) because a shape function satisfies the Kronecker delta function property [6]:

$$\phi_i(\mathbf{r}_j) = \delta_{ij}. \quad (4)$$

By the above property, the values of the interpolation function on the nodes are

$$\hat{u}(\mathbf{r}_j) = \sum_{i=1}^N u_i \phi_i(\mathbf{r}_j) = \sum_{i=1}^N a_i \delta_{ij} = u_j. \quad (5)$$

Note that the nodes for the electric and magnetic fields are scattered separately, as shown in Fig. 2. Thus, the shape functions ϕ^e and ϕ^h are built from the nodes for the electric and magnetic fields, respectively [7]. By using ϕ^e and ϕ^h , the electric field \mathbf{E} and the magnetic field \mathbf{H} are expressed by the shape functions as

$$\hat{\mathbf{E}}^n(\mathbf{r}) = \sum_{k=1}^{N_e} \mathbf{E}_k^n \phi_k^e(\mathbf{r}), \quad (6)$$

$$\hat{\mathbf{H}}^n(\mathbf{r}) = \sum_{l=1}^{N_h} \mathbf{H}_l^n \phi_l^h(\mathbf{r}). \quad (7)$$

Here, the superscript n denotes the number of time steps. In the MTDM, $\mathbf{E}(\mathbf{r}) = (E_x(\mathbf{r}), E_y(\mathbf{r}), E_z(\mathbf{r}))$, $\mathbf{H}(\mathbf{r}) = (H_x(\mathbf{r}), H_y(\mathbf{r}), H_z(\mathbf{r}))$, and each components (x , y , and z) of the electric field \mathbf{E} and the magnetic field \mathbf{H} is present in the same position. In this paper, 2D-TM mode is adopted for the evaluation: $\mathbf{r} = (x, y)$, $\mathbf{E}(\mathbf{r}) = (0, 0, E_z(\mathbf{r}))$, and $\mathbf{H}(\mathbf{r}) = (H_x(\mathbf{r}), H_y(\mathbf{r}), 0)$.

$$\begin{aligned} E_{z,k}^n &= \frac{1-\alpha}{1+\alpha} E_{z,k}^{n-1} \\ &+ \frac{\Delta t/\varepsilon}{1+\alpha} \sum_{l=1}^{N_h} H_{y,l}^{n-\frac{1}{2}} \frac{\partial \phi_l^h}{\partial x}(\mathbf{r}_k) \\ &- \frac{\Delta t/\varepsilon}{1+\alpha} \sum_{l=1}^{N_h} H_{x,l}^{n-\frac{1}{2}} \frac{\partial \phi_l^h}{\partial y}(\mathbf{r}_k), \end{aligned} \quad (8)$$

$$H_{x,l}^{n+\frac{1}{2}} = H_{x,l}^{n-\frac{1}{2}} - \frac{\Delta t}{\mu} \sum_{k=1}^{N_e} E_{z,k}^n \frac{\partial \phi_k^e}{\partial y}(\mathbf{r}_l), \quad (9)$$

$$H_{y,l}^{n+\frac{1}{2}} = H_{y,l}^{n-\frac{1}{2}} + \frac{\Delta t}{\mu} \sum_{k=1}^{N_e} E_{z,k}^n \frac{\partial \phi_k^e}{\partial x}(\mathbf{r}_l). \quad (10)$$

Here, Δt denotes the computation time step and should satisfy the Courant condition. For the delta function property of Eq. (4), the values of the interpolation function on the nodes would be $\hat{E}_z^n(\mathbf{r}_k) = E_{z,k}^n$; the same applies to the magnetic field and other components. In addition, the summation is required in the case of using the partial derivative of

shape functions that are obtained by RPIM, because they do not satisfy the Kronecker delta function property [6]. Parameter α is defined as follows:

$$\alpha = \frac{\sigma \Delta t}{2\varepsilon}. \quad (11)$$

In MTDM, \mathbf{E} and \mathbf{H} are calculated using Eqs. (8), (9), and (10) at each time step, respectively.

2.2 Dispersion model

In the Drude model, the permittivity depends on the frequency of the propagating wave. Thus, the electric flux density in the frequency-space $\bar{\mathbf{D}}$ is defined by the following equation in the dispersion medium:

$$\bar{\mathbf{D}}(\omega) = \bar{\varepsilon}(\omega) \bar{\mathbf{E}}(\omega). \quad (12)$$

Here, ω denotes the angular frequency of the input wave, and the overline denotes the frequency-space function. Applying the inverse Fourier transform to Eq. (12), the time-space function is obtained as follows:

$$\mathbf{D}(t) = \int_0^t \varepsilon(\tau) \mathbf{E}(t-\tau) d\tau. \quad (13)$$

Here, all electromagnetic fields are zero for negative time, because the input field is induced at $t = 0$. The past values of the electric field are stored to calculate Eq. (13) by the integral convolution. In this paper, the RC method is used to reduce the storage cost. In the Drude model, the relative permittivity $\bar{\varepsilon}_r(\omega)$ is defined by

$$\bar{\varepsilon}_r(\omega) = 1 + \frac{\omega_p^2}{i\omega\gamma - \omega^2}, \quad (14)$$

where ω_p denotes the plasma frequency and γ denotes the inverse of the relaxation time. The Drude model is achieved using the RC method, and the electric field is updated using the following equation:

$$\begin{aligned} E_{z,k}^n &= \frac{1}{1+\chi^0} E_{z,k}^{n-1} + \frac{1}{1+\chi^0} \psi_z^{n-1}(\mathbf{r}_k) \\ &+ \frac{\Delta t/\varepsilon_0}{1+\chi^0} \sum_{l=1}^{N_h} H_{y,l}^{n-\frac{1}{2}} \frac{\partial \phi_l^h}{\partial x}(\mathbf{r}_k) \\ &- \frac{\Delta t/\varepsilon_0}{1+\chi^0} \sum_{l=1}^{N_h} H_{x,l}^{n-\frac{1}{2}} \frac{\partial \phi_l^h}{\partial y}(\mathbf{r}_k). \end{aligned} \quad (15)$$

Here, ε_0 denotes the permittivity in vacuum. The convolution summation $\psi_z^{n-1}(\mathbf{r}_i)$ and the initial value of the relative electric susceptibility χ^0 are defined by following equations

$$\psi_{z,k}^{n-1} = E_{z,k}^{n-1} \Delta\chi^0 + e^{-\gamma\Delta t} \psi_{z,k}^{n-2}, \quad (16)$$

$$\psi_{z,k}^0 = 0, \quad (17)$$

$$\chi^0 = \frac{\omega_p^2}{\gamma^2} (\gamma\Delta t - 1 + e^{-\gamma\Delta t}). \quad (18)$$

Moreover, $\Delta\chi^0$ is defined as

$$\Delta\chi^0 = -\frac{\omega_p^2}{\gamma^2} (1 - e^{-\gamma\Delta t})^2. \quad (19)$$

The magnetic field is assumed to be frequency independent. Therefore, the magnetic field is updated by Eqs. (9) and (10).

3. Numerical Evaluation

The effects of the dispersion metal and grooves on the attenuation rate using the 2D-MTDM with the Drude model are investigated. Two types of analytical models are used. The models are shown in Fig. 1. The perfectly matched layer (PML) is adopted for absorbing the boundary conditions on the progressive wave direction [8], and the perfect electric conductor (PEC) is adopted for the boundary conditions of the analysis area. The values of the geometrical parameters used are as follows: The width of the waveguide is $2b + 2d + w$, the length of the straight waveguide is 15λ , the length of the curved waveguide is 5λ , the curvature radius of the curved waveguide is 5.25λ , $b = 0.5\lambda$, $w = \lambda$, $p = 0.5\lambda$, $a = 0.25\lambda$, and $d = 0.25\lambda$, where λ denotes the wavelength of the input wave. Furthermore, the node alignment of the electric and the magnetic fields is shown in Fig. 2. The value of the attenuation rate “ R_A ” used in this paper is defined by the following

equation:

$$R_A = 1 - \frac{\left\langle \int_{\Gamma_{\text{out}}} \mathbf{P} \cdot \mathbf{n}_{\text{out}} d\Gamma \right\rangle_t}{\left\langle \int_{\Gamma_{\text{in}}} \mathbf{P} \cdot \mathbf{n}_{\text{in}} d\Gamma \right\rangle_t}. \quad (20)$$

Here, \mathbf{P} denotes the Poynting vector, \mathbf{n}_{in} denotes the normal vector of Γ_{in} , \mathbf{n}_{out} denotes the normal vector of Γ_{out} , and the values of the attenuation rate R_A are evaluated using the values on the source input line Γ_{in} and the observation line Γ_{out} . Moreover, the bracket $\langle f \rangle_t$ denotes the time average of f . The physical parameters used in this paper are the amplitude of the source wave (1 V/m), the wave speed (3×10^8 m/s), the distance of the neighboring node ($\lambda/40$), the plasma frequency of aluminum ω_p (2.8 PHz) [5], the collision frequency of aluminum (12 THz) [5], the number of layers for PML (24), the dimension of PML (4), and the reflection factor of PML (-120 dB). Besides, the value of E_z is used as the input wave with the equation

$$E_z(\mathbf{r}_{\text{in}}, t) = \beta_1 \begin{cases} \beta_2 \sin(\omega t), & \omega t < 8\pi, \\ \sin(\omega t), & \omega t \geq 8\pi. \end{cases} \quad (21)$$

Here, $\mathbf{r}_{\text{in}} \in \Gamma_s$, and β_1 and β_2 are defined by the following equations:

$$\beta_1 = \sin\left(\frac{r_{x,\text{in}} - (b + d)}{w} \pi\right), \quad (22)$$

$$\beta_2 = \frac{1}{2} \left\{ 1 - \cos\left(\frac{\omega t}{8}\right) \right\}. \quad (23)$$

The following equation is adopted for the radial basis function $F(|\mathbf{r}|)$.

$$F(|\mathbf{r}|) = (|\mathbf{r}|^2 + R^2)^{-0.5}. \quad (24)$$

Here, the value of the support radius R is $2l_{\text{min}}$, where l_{min} denotes the minimum distance between the nodes.

First, it was verified if the Drude model was embedded correctly. The value of the reflection rate when the plane wave is vertically generated against the dispersive wall is plotted as a function of the input wave frequency in Fig. 3. We can see from this figure that the reflection rate is calculated with high precision because the analytical solution and the simulation results are almost identical. In addition, the reflection rate is reduced when the frequency of the input wave is greater than the plasma frequency.

Second, the influence of the grooves on the attenuation rate in the straight waveguide is investigated. The values of the attenuation rate R_A are plotted as a function of the input wave frequency in Fig. 4. We see from this figure that the values of the attenuation rate are changing irregularly because the waves penetrate into the metal for $\omega/\omega_p > 1$. In addition, the attenuation rate is negative because the denominator of Eq. (20) increases for waves at approximately Γ_{in} that penetrate deeply into the metal compared to those at approximately Γ_{out} . This difference is not observed in

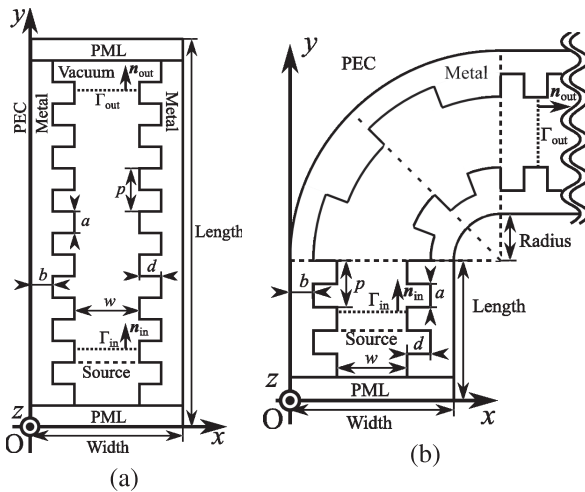


Fig. 1 Conceptual diagrams of the corrugated waveguide: (a) straight waveguide and (b) right-angle waveguide.

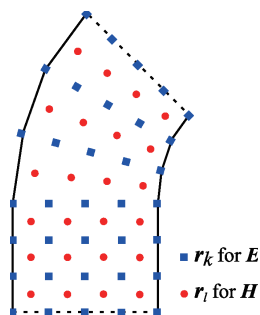


Fig. 2 Conceptual diagram of the nodes alignment in the waveguide.

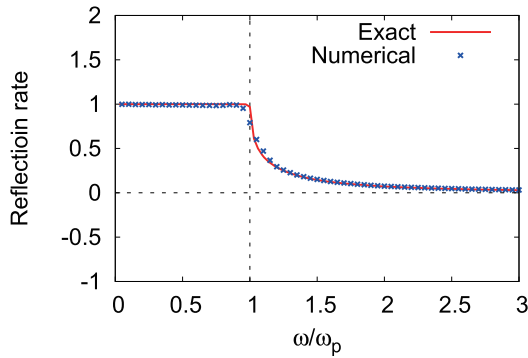


Fig. 3 Reflection rate of the plane wave. The wave is vertically generated against the dispersive wall.

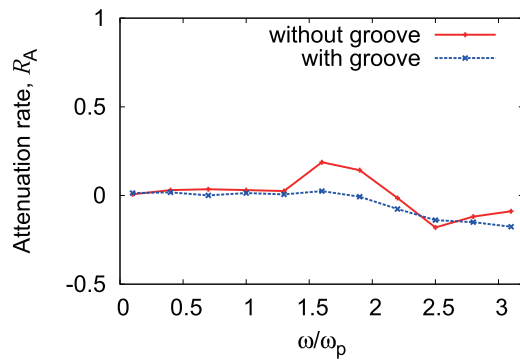


Fig. 4 The values of attenuation rate R_A plotted as a function of input wave frequency in the straight waveguide.

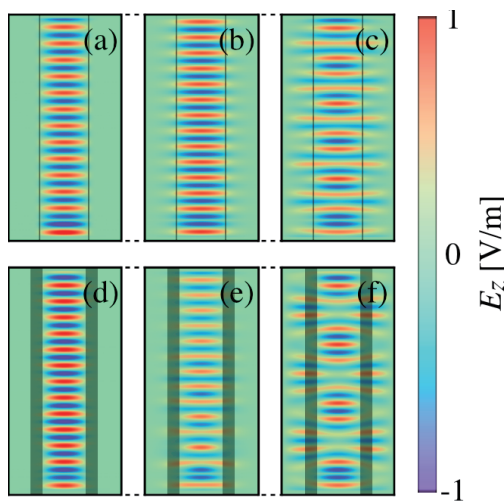


Fig. 5 Distribution of the electric field E_z in the straight waveguide. The gray background indicates the area of the corrugated groove, or the boundary of the vacuum and the metal. (a), (b), and (c) without groove, (d), (e), and (f) with groove, (a), (d) $\omega/\omega_p = 0.1$, (b), (e) $\omega/\omega_p = 1$, and (c), (f) $\omega/\omega_p = 3$.

the distributions of the waveguide with grooves and without grooves for $\omega/\omega_p = 0.1$ (see Figs. 5 (a) and 5 (d)). In the waveguide without grooves, periodic distribution is ob-

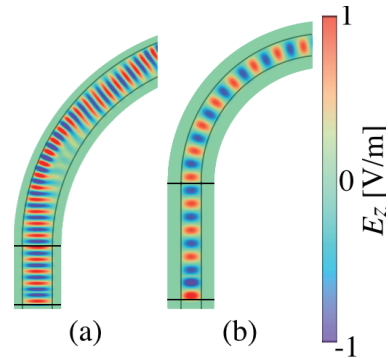


Fig. 6 Distribution of the electric field E_z in the curved waveguide without groove. The gray background is the boundary of the vacuum and the metal. $\omega/\omega_p = 1$, (a) $w = 3\lambda$ and the curvature radius is 15.75λ and (b) $w = \lambda$ and the curvature radius is 5.25λ .

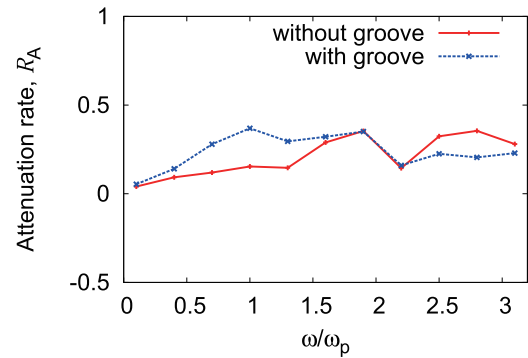


Fig. 7 The values of attenuation rate R_A plotted as a function of the input wave frequency in the curved waveguide.

tained (see Fig. 5 (b)), although a distorted waveform is observed for $\omega/\omega_p > 1$ (see Fig. 5 (c)). On the other hand, we can see from Figs. 5 (e) and 5 (f) that the distorted waveforms are observed even if $\omega/\omega_p > 1$; this is induced by the corrugated waveguide.

Next, we investigate the influence of the width of the curved waveguide without grooves on the electromagnetic wave propagation as a run-up to evaluate the attenuation rate. The distribution of the electric field E_z in the waveguide is shown in Fig. 6 for $\omega/\omega_p = 1$. In the case of $w = 3\lambda$ (see Fig. 6 (a)), the incident wave is reflected on the waveguide wall. On the other hand, the wave propagates while maintaining the waveform in the case of $w = \lambda$ (see Fig. 6 (b)). This is due to the larger cutoff frequency owing to the narrowing width of the waveguide.

Finally, we evaluate the values of attenuation rate R_A in the curved waveguide. The attenuation rate R_A is plotted as the function of the corrugated channels in the curved waveguide (see Fig. 7). The distributions of the electric field E_z in the waveguide is shown in Fig. 8. From Figs. 7 and 8, we see that the corrugated waveguide is strongly affected by the dispersion metal of the waveguide wall more than the waveguide without grooves, similar to the straight

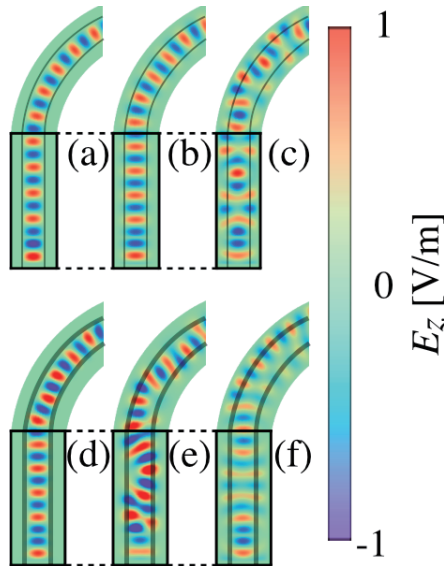


Fig. 8 Distribution of the electric field E_z in the curved waveguide. The gray background denotes the area of the corrugated groove or the boundary of the vacuum and the metal. (a), (b), and (c) without groove, (d), (e), and (f) with groove, (a), (d) $\omega/\omega_p = 0.1$, (b), (e) $\omega/\omega_p = 1$, and (c), (f) $\omega/\omega_p = 3$.

waveguide. In addition, the transmission loss of the curved waveguide is greater than that of the straight waveguide because the incident wave is reflected on the waveguide wall.

4. Conclusion

We have developed a numerical code for analyzing

the electromagnetic wave propagation in complex-shaped waveguide. In addition, we have evaluated the influence of the dispersion metal on the attenuation rate. The conclusions are summarized as follows:

1. In the case of the curved waveguide without grooves, the wave was propagated along the narrow width of the waveguide because the cutoff frequency increased.
2. In both the straight and curved waveguides, the wave propagating in the waveguide with the grooves penetrated deep into the metal compared with the waveguide without grooves.
3. The transmission loss for the curved waveguide was greater than in the case of the straight waveguide because the incident wave was reflected on the waveguide walls.

Acknowledgment

This work is supported by KAKENHI (24656560). The authors wish to thank Dr. A. Takayama for the helpful discussions.

- [1] M. Fujiwara *et al.*, *J. Fusion Energy* **15**, 7 (1996).
- [2] Y. Fujita *et al.*, *J. Plasma Fusion Res.* **8**, 2401061 (2013).
- [3] N. Kashima *et al.*, *Jpn. J. Appl. Phys.* **52**, 11ND02 (2013).
- [4] H. Nakamura *et al.*, *J. Phys.: Conf. Ser.* **410**, 012046 (2013).
- [5] R.D. Radic *et al.*, *Appl. Opt.* **37**, 22, 5271 (1998).
- [6] G.R. Liu *et al.*, *Comput. Mech.* **36**, 421 (2005).
- [7] T. Kaufmann *et al.*, *IEEE Trans. Microw. Theory Tech.* **58**, 3399 (2010).
- [8] J.-P. Berenger *et al.*, *J. Comput. Phys.* **114**, 185 (1994).